Testing the independence law of partial ARMs: implications for paleointensity determination

Yongjae Yu *, David J. Dunlop, Özden Özdemir

Geophysics, Department of Physics, University of Toronto, 60 st. George Street, Toronto, M5S 1A7, Canada

Abstract

The independence of partial anhysteretic remanent magnetizations (pARMs) was tested by alternating field demagnetizing orthogonal pARMs whose blocking field intervals do not overlap with each other. Experimentally the two pARMs demagnetized independently for single-domain grains but for multidomain and pseudo-single-domain grains, a superimposed remanence significantly affected the demagnetization of the pre-existing remanence. Experimentally and in numerical simulations, when a total anhysteretic remanent magnetization (simulating primary remanence in a field H_a) was orthogonally overprinted by pARM (simulating remagnetization in H_b), estimation of the intensity of H_b was relatively successful but the intensity of H_a was always underestimated. Conversely, the direction of H_a was preserved but the direction of H_b was spurious. These striking results are caused by the violation of the pARM independence law, implying that the conventional sample rejection criteria in pseudo-Thellier paleointensity determination require modification.
© 2003 Elsevier Science B.V. All rights reserved.

1. Introduction

In order to extract relative paleointensity information from sedimentary sequences (carrying mostly post-depositional remanence), a pseudo-Thellier method that avoids heating, and thus chemical alteration, was developed by Tauxe et al. [1] and has been widely used [2–7]. The pseudo-Thellier method compares increments of natural remanent magnetization (NRM) remaining in a series of alternating-field (AF) demagnetization steps with increments of partial anhysteretic remanent magnetization (pARM) acquired in a laboratory field in matching AF steps. A fundamental difference compared to the Thellier method is that thermal effects are omnidirectional, whereas pARM and AF demagnetization have a specific direction. The effectiveness of demagnetization depends on the angle between the NRM and the AF.

Thellier-type [8] paleointensity determinations are based on the validity of the laws of additivity, reciprocity, and independence of partial thermo-remanent magnetization (pTRM) [9]. The main

---

* Corresponding author. Tel.: +1-905-828-5440;
Fax: +1-905-828-3717.
E-mail address: yjyu@physics.utoronto.ca (Y. Yu).

purpose of this paper and two previous ones [10,11] is to test the analogous laws of additivity, reciprocity, and independence of pARM. Only if these laws of pARM are valid is it justifiable to use ARM paleointensity methods. Additivity of pARMs has been shown to be obeyed for all samples, regardless of grain size, lithology, and Ti composition [10]. On the other hand, the reciprocity of pARMs, i.e. unblocking field = blocking field, was fully satisfied only for single-domain (SD) and small pseudo-single-domain (PSD) magnetites and rocks or sediments containing them [11]. The aim of the present paper is to test the independence of pARMs, namely that a pARM $(\tilde{H}_2,\tilde{H}_1)$ produced by a steady field applied over the AF interval $(\tilde{H}_2,\tilde{H}_1)$, must be independent of pARMs produced over field intervals that do not overlap $(\tilde{H}_2,\tilde{H}_1)$. Any violation of the independence law compromises the quality of paleointensity determination.

We tested the independence of pARMs added in orthogonal pairs and in orthogonal sets of three. Testing independence using non-parallel pairs of pARMs is necessary for two reasons. First, during pARM acquisition in the pseudo-Thellier method, the field is applied along the cylindrical axis of the sample, which is generally not the NRM direction. Second, superposition of pARM on ARM is analogous to partial replacement of TRM by pTRM, mimicking the remagnetization process in nature. If the pARMs are truly independent, producing them along orthogonal axes permits each to be tracked separately.

2. Samples and experiments

Eight synthetic samples were prepared using magnetite powders whose mean grain sizes range from single domain (SD, 0.065 μm) to small multidomain (MD, 18.3 μm) [10]. These samples are 0.5% by volume dispersions of magnetite in a matrix of CaF_2. Cylindrical pellets 8.8 mm in diameter and 8.6 mm in height were pressed and then tightly wrapped with quartz wool inside quartz capsules. The capsules were sealed under vacuum and annealed for 3 h at 700°C. The magnetic properties, including ARM and TRM intensities,

did not change significantly after annealing (Table 1).

Twenty-six natural samples were also studied: two andesites and one red-scoria [12], 14 gabbros [13,14], three granites [15,16], and six freeze-dried lake sediments [5]. The natural samples selected have magnetic and paleomagnetic properties that are well documented. They were chosen from a much larger collection of several hundred cores on the basis of their low magnetic fabric anisotropy, their reproducible ARM and TRM intensities (for sediments, ARM only), and minimal viscous magnetic changes. In particular, low fabric anisotropy is necessary to produce orthogonal remanences by applying orthogonal fields. The gabbros and lake sediments had yielded reliable paleointensities from the Thellier and pseudo-Thellier methods, respectively (Table 2).

The most straightforward way to test independence is by observing the demagnetization behavior of multiple orthogonal pARMs with non-overlapping blocking field intervals. We tested multivectorial remanences of three types. The first two are bivectorial and the third is trivectorial.

2.1. Bivectorial test 1

We produced $pARM_z$ (100 mT, $\tilde{H}_i$), with a steady field **H** applied along z from 100 mT to $\tilde{H}_i$ and zero field from $\tilde{H}_i$ to 0 mT, yielding a

Table 1
Synthetic samples

Sample	Powder	d (μm)
1	4000	0.065
2	5099	0.21
3	112978	0.44
4	M	0.24
5	5000	0.34
6	3006	1.06
7	112982	16.9
8	041183	18.3

Powders 4000, 112978, 5000, 3006, 112982, and 041183 are from the Wright Company; powders 5099 and M are the products of Pfizer and Mapico companies. The estimated mean grain size d was determined using scanning electron microscope (SEM). More than 1000 grains were typically counted from at least six SEM photos per powder.

vector M_1, using a Molspin AF demagnetizer. Then to M_1, we added pARM$_x$ ($\tilde{H}_i$, 0) produced by H applied along x from $\tilde{H}_i$ to 0 mT. The resultant vector sum is M_2.

2.2. Bivectorial test 2

In this experiment, we first produced total ARM$_z$ (100 mT, 0) and then partially overprinted this by pARM$_x$ ($\tilde{H}_i$, 0), giving a vector resultant M_3. The processes leading to M_1, M_2, and M_3 are illustrated in Fig. 1. M_2 and M_3 were repeated for six different $\tilde{H}_i$ values: 10, 20,...,60 mT.

2.3. Trivectorial test

In a further experiment, we again produced M_3 and then partially overprinted it by a third pARM$_y$ ($\tilde{H}_j$, 0), with $\tilde{H}_j < \tilde{H}_i$, giving M_4 (not illustrated in Fig. 7).

Double AF demagnetization [$\pm x$, $\pm y$, $\pm z$] was carried out in 5 mT increments for M_2, M_3, and M_4. M_4 used the same $\tilde{H}_i$ as M_3, and $\tilde{H}_j = \tilde{H}_i/2$.

3. Comparison of component intensities

In the ideal case, M_1 isolates the coercivity or blocking field fraction (100 mT, $\tilde{H}_i$). If M_1 is independent of the non-overlapping pARM$_x$ ($\tilde{H}_i$, 0), the components z_1 and z_2 of M_1 and M_2 should be identical. The case of M_3 is similar, but a little different. The total ARM aligns all coercivity fractions from 0 to 100 mT along z.

Table 2
Natural samples

Sample	Ref.	T_{UB} (°C)
An-ei basalts	[9]	580
Kometsuka red-scoria	[9]	500
Tudor Gabbro	[10]	580
Cordova Gabbro	[11]	580
Burchell Lake Granite	[12]	580
Shelley Lake Granite	[13]	580
Lake Pepin sediments	[14]	n.a.

Ref. is the reference; T_{UB} is the maximum unblocking temperature from the thermal demagnetization of sister specimens; n.a. is not available.
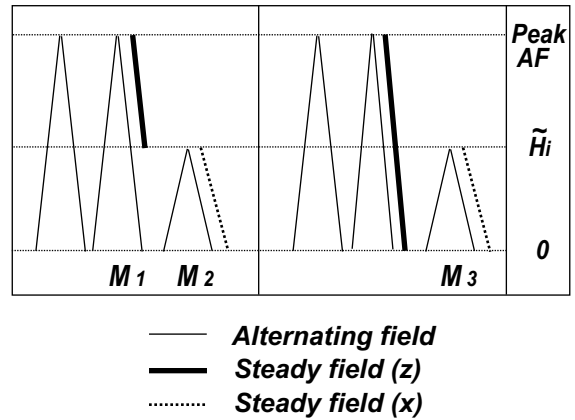

Fig. 1. A schematic diagram for bivectorial tests 1 and 2.

The later superimposed pARM$_x$ ($\tilde{H}_i$, 0) should redirect the coercivity fraction ($\tilde{H}_i$, 0) along x, leaving the fraction (100 mT, $\tilde{H}_i$) untouched. Therefore, we expect ideally to find $z_3 = z_2$ and $x_3 = x_2$. As long as the independence law is satisfied, z_1, z_2, and z_3 should have the same values regardless of their experimental sequences, and the same is true of x_2 and x_3.

The ratios z_3/z_1 and z_2/z_1 are plotted as a function of $\tilde{H}_i$ for synthetic samples in Fig. 2a,b. As the value of $\tilde{H}_i$ increases, z_3/z_1 decreases (Fig. 2a), suggesting that coercivity fraction (100 mT, $\tilde{H}_i$) is less independent of fraction ($\tilde{H}_i$, 0) at higher $\tilde{H}_i$. A similar trend is seen for z_2/z_1 vs $\tilde{H}_i$ (Fig. 2b). For example, for the 0.065-μm SD sample, 91% of pARM$_z$ (100 mT, 30 mT) is independent of pARM$_x$ (30 mT, 0) while only 64% of pARM$_z$ (100 mT, 60 mT) is independent of pARM$_x$ (60 mT, 0) (Fig. 2b). For the 16.9-μm and 18.3-μm MD samples, more than half of pARM$_z$ (100 mT, $\tilde{H}_i$) was erased by pARM$_x$ ($\tilde{H}_i$, 0) for $\tilde{H}_i > 40$ mT (Fig. 2b). In all cases, even for the 0.065-μm SD sample, the ratios of z_2/z_1 were significantly lower at higher $\tilde{H}_i$ values than z_3/z_1 ratios, showing that the remanence acquisition processes of M_2 and M_3 are not entirely equivalent.

In the natural samples, Km 3 (red-scoria, [12]) shows similar behavior to that of the 0.065-μm SD sample, indicating that the magnetic carriers in Km 3 are SD magnetites (Fig. 2c,d). Samples 456 A (sediments, Lake Pepin, MN, USA [5]), C 12 (Cordova Gabbro, [14]), and An 1 (An-ei
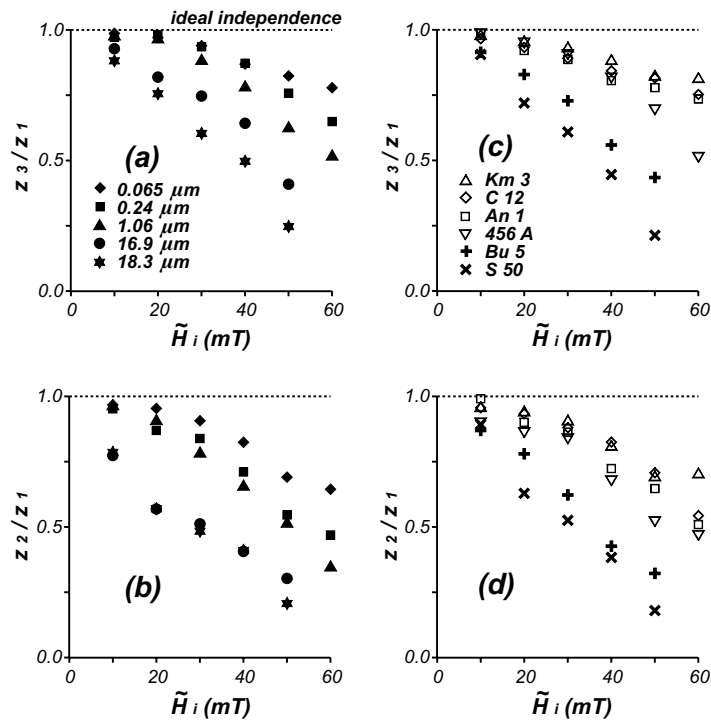
Fig. 2. The ratios z_3/z_1 and z_2/z_1 versus $\tilde{H}_i$ for synthetic and natural samples.

andesite, [12]) gave results similar to those of synthetic PSD magnetites. The granites Bu 5 (Burchell Lake Granite [15]) and S 50 (Shelley Lake Granite [16]) have the smallest ratios z_3/z_1 (Fig. 2c) and z_2/z_1 (Fig. 2d). Large MD grains must be responsible for the very significant drops of z_2/z_1 and z_3/z_1 in these granites.

4. Demagnetization behavior

Results of AF demagnetization of M_3 ($\tilde{H}_i = 20$, 40 mT for Fig. 3a and 20, 60 mT for Fig. 3b) are shown in normalized vector plots. The results for AF steps $> \tilde{H}_i$ fall on the vertical axis and are omitted for clarity.
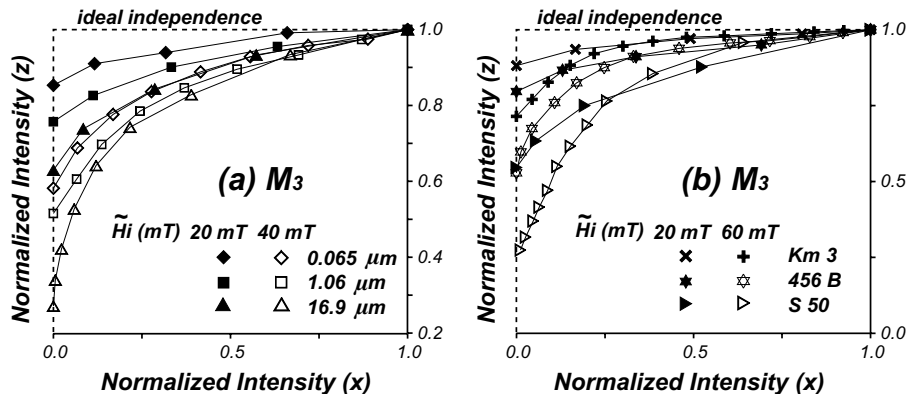

Fig. 3. AF demagnetization of M_3 for (a) synthetic and (b) natural samples.
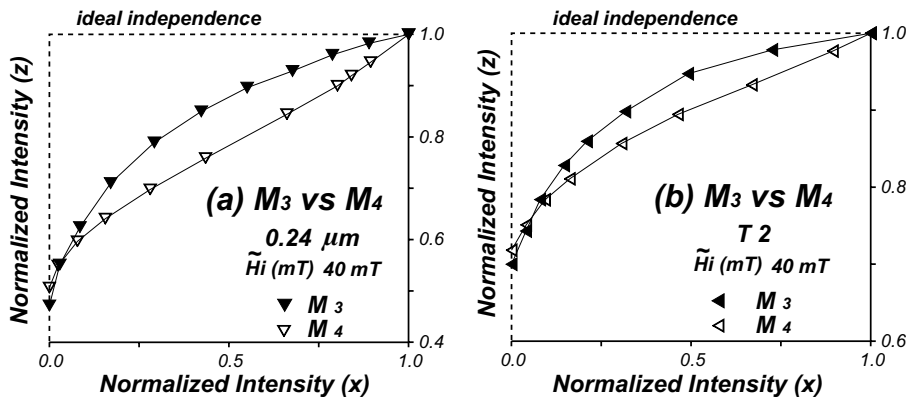
Fig. 4. Comparison of AF demagnetization of M_3 and M_4 for (a) synthetic 0.24 μm magnetite and (b) Tudor Gabbro sample T 2.

For synthetic samples, M_3 ($\tilde{H}_i = 20$ mT) decays continuously regardless of the grain size (Fig. 3a). The SD sample (0.065 μm) comes closest to obeying independence, with 85% of z_3 left at $\tilde{H}_i = 20$ mT compared to 76% and 63% for PSD (1.06 μm) and MD (16.9 μm) samples. AF demagnetization of M_3 ($\tilde{H}_i = 40$ mT) gives an arch-shaped decay curve with only 58%, 52%, and 27% of z_3 left at $\tilde{H}_i = 40$ mT (Fig. 3a). Whatever the value of $\tilde{H}_i$, less of z_3 was left at $\tilde{H}_i$ as the grain size increased. Corresponding AF demagnetization plots of M_3 ($\tilde{H}_i = 20$ mT) for Km 3, 456 B, and S 50 resemble those of the synthetic samples, indicating that their predominant remanence carriers are SD, PSD, and MD magnetite (Fig. 3b).

The AF demagnetization responses of M_3 ($\tilde{H}_i = 40$ mT) and M_4 ($\tilde{H}_i = 40$ mT) are different for PSD samples. M_4 has a quasi-linear vector plot while M_3 has a continuously curving vector plot (Fig. 4a,b), showing that pARM$_y$ (20 mT, 0) alters the coercivity distribution of pre-existing remanences. This interesting behavior is also noticeable for some natural PSD samples. On the other hand, AF demagnetization plots for M_3 ($\tilde{H}_i = 40$ mT) and M_4 ($\tilde{H}_i = 40$ mT) are similar, for synthetic SD and MD samples, for Km 3 (SD characteristics), and for granite samples (MD characteristics). The fractions of M_3 and M_4 remaining after AF demagnetization to $\tilde{H}_i$ were almost identical for all the samples used, regardless of their grain sizes and lithologic variation (Fig. 4a,b).

5. Violation of independence and paleointensity determination

5.1. Multivectorial paleointensity simulations

Arai plots [17] are widely used in paleointensity determination studies but conventional Arai plots are unable to represent multivectorial properties. Multivectorial Arai plots were introduced for Thellier-type paleointensity determinations in order to overcome this limitation [14]. In this section, the consequences of the violation of the pARM independence law on analogous Arai-type plots for pARMs will be investigated numerically.

For mathematical convenience, we at first assume ideal behavior, namely that additivity and reciprocity of pARMs are valid. As part of experimental sequence M_3, each sample acquires a total ARM$_z$ in field H_a. In the modeling, all results will be normalized to ARM$_z$; thus ARM$_z$ has the vectorial representation [0,0,1]. Since pARM$_x$ ($\tilde{H}_i$, 0), produced in field H_b, replaces a fraction $(1-p)$ of ARM$_z$, the resultant M is [$r(1-p)$, 0, tp] where p is the remaining fraction of ARM$_z$, r is the ratio of H_b/H_a, and t represents the degree of independence (see Fig. 5 insets, which are modeled on the M_4 vector plots of Fig. 4; $t = 1$ means total independence).

We now simulate pseudo-Thellier paleointensity determination for a bivectorial NRM $M_3 = pM_1 + M_2$. First consider pure ARM$_z$, as produced ini-
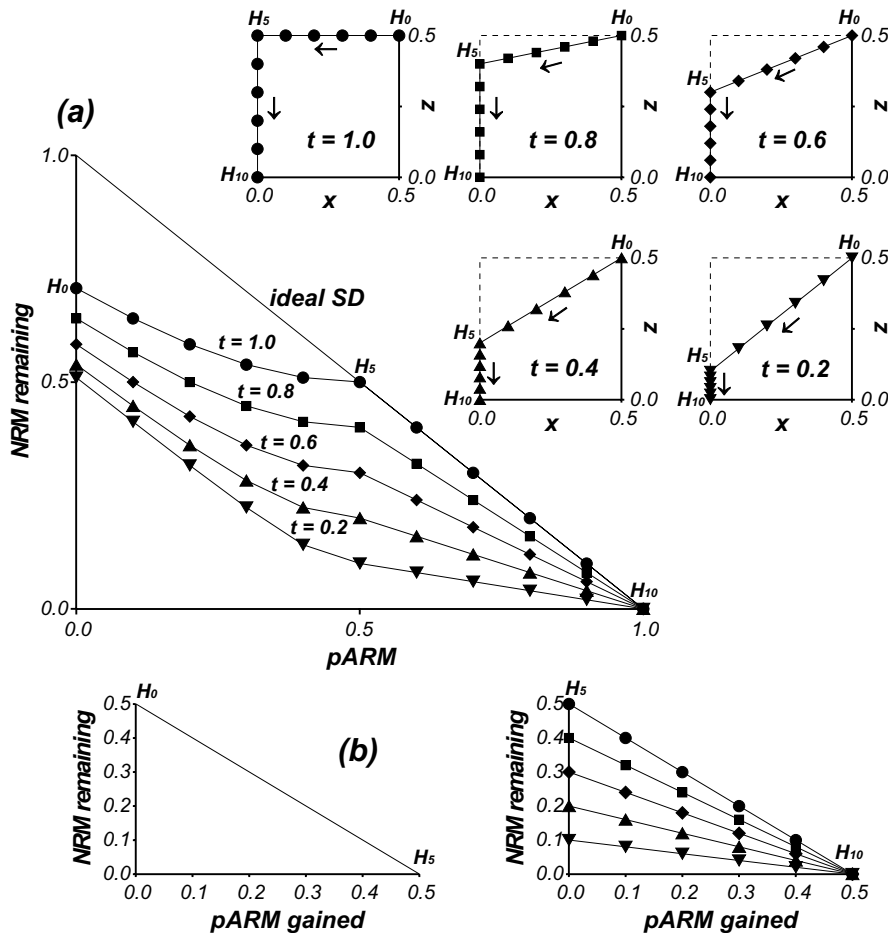
Fig. 5. (a) Numerically predicted Arai-type plots with associated vector projections. The values of t denote the degree of independence. (b) Vectorially separated Arai-type plots for overprinting (left) and primary (right) remanences.

tially as part of M_3. Suppose 10 AF steps $\tilde{H}_i$ ($i = 1$ to 10) are defined so that each step increment in AF demagnetization destroys 10% of ARM_z. According to the reciprocity law, these $\tilde{H}_i$'s should also produce 10% step increments of pARM during remanence acquisition steps. Thus, NRM remaining versus pARM acquisition for these 10 AF steps would fall on the ideal SD line in the conventional Arai plot (see ideal line in Fig. 5).

In the modeling process, for simplicity, we assume that $pARM_x$ was acquired at AF step $\tilde{H}_5$ ($P = 0.5$), so that the intensity of $pARM_x$ is one-half of ARM_z when $r = 1$. AF steps $\tilde{H}_1$–$\tilde{H}_5$ demagnetize equal 20% increments of $pARM_x$ and

steps $\tilde{H}_6$–$\tilde{H}_{10}$ demagnetize 20% increments of $p^\bullet$ (ARM_z).

The effect of the violation of independence is illustrated in conventional Arai-type plots with associated vector projections for $r = 1$ in Fig. 5a. As the values of t decrease, i.e., as independence is increasingly violated, the overall shapes of Arai-type plots change from convex-up to convex-down. The portion $\tilde{H}_i < \tilde{H}_5$ is always curved for all values of t. In order to overcome this limitation, separate vector Arai plots were constructed. The NRM remaining at $\tilde{H}_5$ (namely pM_a) was vectorially subtracted from all NRMs M for AF steps $\tilde{H}_i < \tilde{H}_5$, giving adjusted values NRM' (namely M_b). No adjustment is needed for
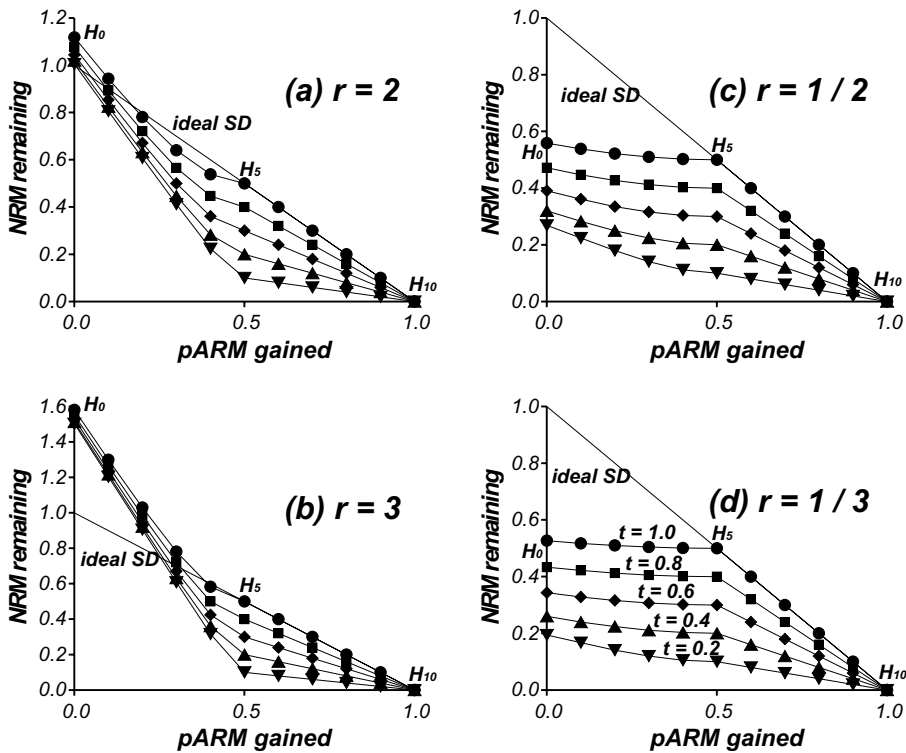
Fig. 6. Simulated Arai-type plots for field ratios (a) $r = 2$, (b) $r = 3$, (c) $r = 1/2$, and (d) $r = 1/3$. Symbols as in Fig. 5.

pARMs because these are acquired in the same laboratory field direction below and above $\tilde{H}_5$. Then the Arai plot for M_b is NRM′ vs pARM, over the range 0–$\tilde{H}_5$. The Arai plot for pM_a, over the range $\tilde{H}_5$–100 mT, is NRM vs. [pARM$-$pARM($\tilde{H}_5$)]. The latter subtraction is a simple scalar one. In practice, constructing separate Arai plots requires a priori information, the AF step $\tilde{H}_i'$ ($= \tilde{H}_5$ in the present modeling) at which M_b and pM_a have a sharp junction in vector projections. We can infer the values of $\tilde{H}_i'$ directly from the Arai plot or from paleomagnetic vector projections.

The recalculated vectorial Arai plots reveal correct paleointensities for H_b (with slope -1 in Fig. 5b, left) but fail to estimate correct paleointensities for H_a (Fig. 5b, right). The paleointensities for H_a are underestimated by a factor t (only $t = 1$ gives a correct intensity). For example, $t = 0.6$ gives an apparent field intensity that is 60% of the true value.

Similar simulations for other values of r appear in Fig. 6. The vector projections are omitted because they are similar to those in Fig. 5a. In general, convex-down shapes prevail for $r > 1$ while convex-up dominates for $r < 1$ (Fig. 6). Although not shown, the separated vectorial Arai-type plots again give correct paleointensities for H_b (with the slope corresponding to r) but yield slopes and paleointensities for H_a that are a factor t low.

5.2. Multivectorial paleointensity experiments

In order to bridge from numerical simulations to reality, we carried out experimental pseudo-Thellier analyses on our samples. First, M_3 was produced using $\tilde{H}_i = 40$ mT for $r = 1$ ($H_a = H_b$). Then, stepwise AF demagnetization and matching pARM acquisition were carried out on M_3, usually with 5 mT step increments. We will denote these results as experiment 1. Based on Fig. 2a, $\tilde{H}_i = 40$ mT was used since the ratio z_3/z_1 starts to show a great deviation between SD and PSD samples above this field.
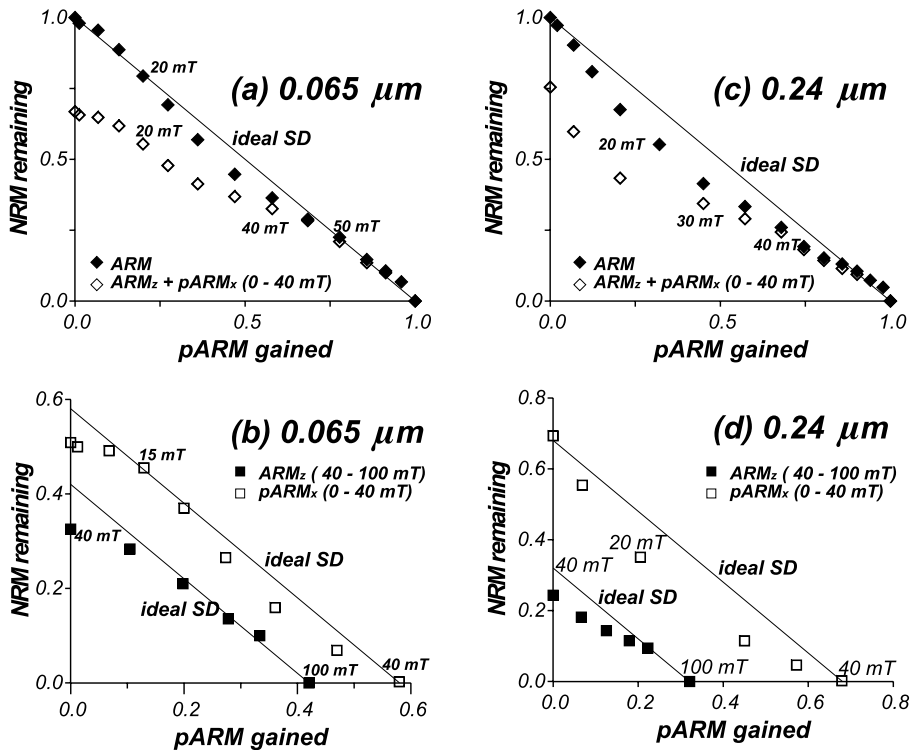
Fig. 7. Experimental pseudo-Thellier results for synthetic magnetites. (a, b) 0.065 μm, (c, d) 0.24 μm. (a, c) are conventional Arai plots. (b, d) are vectorially separated Arai plots.

In Figs. 7 and 8, the results are compared to pseudo-Thellier experiments (denoted as experiment 2) on total ARM. For experiment 1, the separated multivectorial Arai plots are also provided (Figs. 7b,d and 8b,8d). For a fixed $\tilde{H}_i = 40$ mT, p varied but was usually ~ 0.3–0.4. In order to check the reproducibility, experiments 1 and 2 were replicated four times. The results were repeatable within experimental errors.

The results for synthetic SD grains are the most encouraging. Experiments 1 and 2 converge at $\tilde{H}_i = 40$ mT in the conventional Arai plot (Fig. 7a), as expected from the numerical modeling (Fig. 5). For experiment 1, the vectorially corrected Arai plots yield correct intensities for both H_a and H_b (Fig. 7b). However, the synthetic PSD samples show different aspects (Figs. 7c and 7d). First, H_b cannot be determined because the plot is curved, although the two end points lie on the ideal SD line (Fig. 7d). Second, H_a was underestimated by $\sim 20\%$.

The experiments using the natural samples are worthy of note. Both An 1 and 456 A show convergence at $\tilde{H}_i = 40$ mT (Fig. 8a,c), like the synthetic SD and PSD samples. However, typical PSD behavior of non-linear, convex-down curves in experiment 2 persists in the vectorially corrected Arai plots and correct paleointensities cannot be found. Regardless of the grain size and lithology of the samples, all the experimental results in Figs. 7 and 8 converge at $\tilde{H}_i'$.

6. Discussion

6.1. Comparison of component intensities

Ideally the intensities of z_1, z_2, and z_3 should be identical (Section 3). However, experimentally this is not the case. First, values of z_1, z_2, and z_3 are all different from one another, indicating they are isolating different coercivity fractions. Second, the
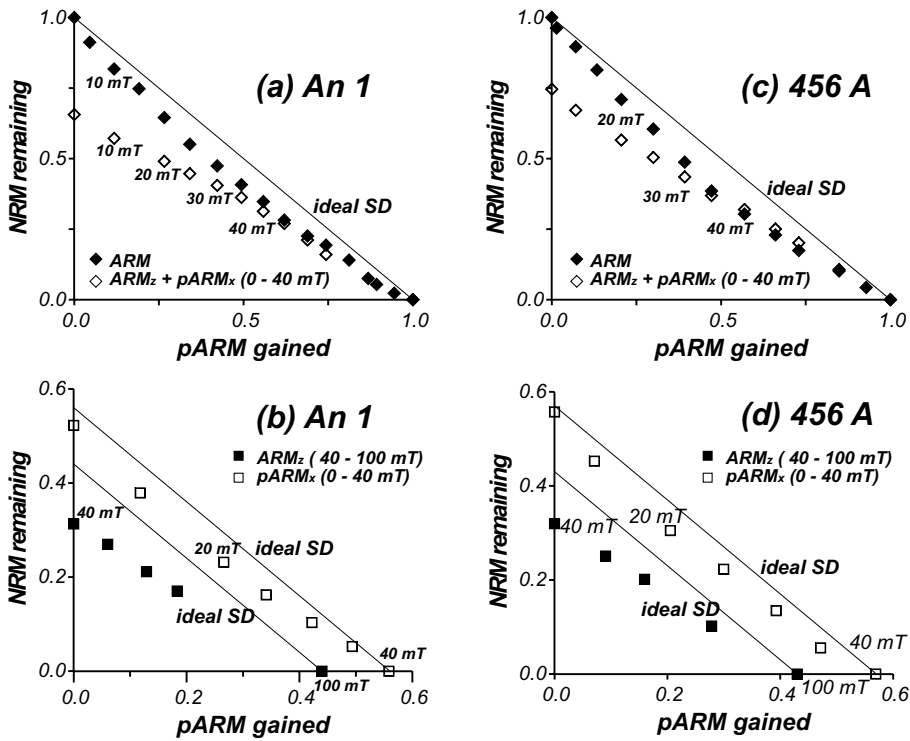
Fig. 8. Experimental pseudo-Thellier results for natural samples. (a, b) An 1, (c, d) 456 A. (a, c) are conventional Arai plots. (b, d) are vectorially separated Arai plots.

relative intensities are always $z_1 > z_3 > z_2$. Third, the coercivity fraction (100 mT, $\tilde{H}_i$) is less independent of the fraction ($\tilde{H}_i$, 0) as the values of $\tilde{H}_i$ increase (Fig. 2). In other words, contrary to intuition, the soft coercivity fraction comes closer to obeying the independence law than the hard coercivity fraction.

6.1.1. Why is $z_1 > z_2? > z_2$?

During AF demagnetization experiments on pARM ($\tilde{H}_b$, $\tilde{H}_a$), it was found that pARM ($\tilde{H}_b$/ AC >, $\tilde{H}_a$) can be represented as the sum of the reciprocal fraction [$\tilde{H}_a < \tilde{H}_{UB} < \tilde{H}_b$] and a low-coercivity tail [$\tilde{H}_{UB} < \tilde{H}_a$] [11]. Similarly in bivectorial test 1, pARM$_z$ (100 mT, $\tilde{H}_i$) has a reciprocal fraction [$\tilde{H}_i < \tilde{H}_{UB} > 100$ mT] and a low-coercivity tail [$\tilde{H}_{UB} < \tilde{H}_i$]. When pARM$_x$ ($\tilde{H}_i$, 0) was later added, we expect pARM$_x$ to affect not only the previously unmagnetized coercivity fraction ($\tilde{H}_i$, 0) but also the low-coercivity tail [$\tilde{H}_{UB} < \tilde{H}_i$] of pARM$_z$ (100 mT, $\tilde{H}_i$). Although

pARM$_x$ is producing remanence rather than erasing remanence as in AF demagnetization with no biasing field, the unblocking coercivity fraction of [$\tilde{H}_{UB} < \tilde{H}_i$] is affected similarly by the AF in both cases, as will be shown in Section 6.2. Thus, the reason z_2 (M_2) is smaller than component z_1 (M_1) is because pARM$_x$ ($\tilde{H}_i$, 0) erases the low-coercivity tail [$\tilde{H}_{UB} < \tilde{H}_i$] of pARM$_z$ (100 mT, $\tilde{H}_i$).

6.1.2. Why is the soft coercivity fraction more independent?

The low-coercivity tail provides the answer to this question as well. Yu et al. [11] reported that the low-coercivity tail of pARM is more prominent at higher $\tilde{H}_i$, i.e., reciprocity was more seriously violated at higher $\tilde{H}_i$. Larger low-coercivity tails are responsible for less independent hard coercivity fractions.

6.1.3. Why is $z_3 > z_2? > z_2$?

The result $z_3 > z_2$ is unanticipated, since both

total ARM_z and $pARM_z$ (100 mT, $\tilde{H}_i$) were over-printed by the same $pARM_x$ ($\tilde{H}_i$, 0). The explanation must be that total and partial ARMs are overprinted in non-equivalent ways. In the ideal case, M_1 isolates coercivity fraction (100 mT, $\tilde{H}_i$) along z, and then in M_2, coercivity fraction ($\tilde{H}_i$, 0) is aligned along x. On the other hand, for M_3, the total ARM orients the entire coercivity fraction (100 mT, 0) along z, and later $pARM_x$ will redirect the coercivity fraction ($\tilde{H}_i$, 0) along x. The low-coercivity tail of $pARM_z$ (100 mT, $\tilde{H}_i$) seems not to be a factor since $pARM_x$ was produced equivalently for both M_2 and M_3. Experimentally we observed that x_2 and x_3 were always identical within experimental errors. The equality of x_2 and x_3 regardless of the grain size or lithology of samples proves the equivalence of $pARM_x$ ($\tilde{H}_i$, 0) in the two cases. Systematically higher intensities of z_3 indicate that the coercivity fraction (100 mT, $\tilde{H}_i$) of the total ARM_z is more AF resistant than $pARM_z$ (100 mT, $\tilde{H}_i$). It is possible that M_3 generates stronger pinning of domain walls than M_1 for the coercivity fraction (100 mT, $\tilde{H}_i$) but there are no microscopic observations or micromagnetic calculations on the domain states of pARMs relevant to these experiments.

6.2. Demagnetization behavior

The experiments on the demagnetization of superimposed pARMs used M_3 rather than M_2 since M_3 is more relevant to the remagnetization process in nature. In addition, M_3 is less dependent on $pARM_x$ than M_2 (Fig. 2).

The AF demagnetization behavior of the synthetic samples yielded a strong grain-size dependence. The large low-coercivity tail in the coercivity spectrum of pARM of MD grains results in a significant portion of the overprinted remanence (i.e. z_3) being AF demagnetized well below $\tilde{H}_i$ (Fig. 3a). As a result, AF demagnetization of PSD and MD grains shows less orthogonality compared to SD grains. A further loss of orthogonality occurs when an additional $pARM_y$ is superimposed (Figs. 4a,b), implying that multiple superposition of remanences in low coercivity intervals can significantly affect intermediate to hard coercivity fractions.

Normalized vector plots are convenient for stacking data from different $\tilde{H}_i$ values or from different samples, but they give a misleading picture of vector directions when x and z components have different intensities (Fig. 3). For example, estimated values of inclination I for the 0–20 mT interval for the 0.065 µm and 16.9 µm samples are 20.7° and 8.2°, respectively. On the other hand, it was the 0.065 µm sample which gave better independence, i.e., lower z_3/x_3 after 20 or 40 mT demagnetization, in a normalized vector plot (Fig. 3a). This apparent paradox results from the very different starting intensity ratios of x- and z-components for SD ($x_3/z_3 = 0.37$) and MD ($x_3/z_3 = 2.40$).

Yu et al. [11] reported that there were no high-coercivity tails in the coercivity distribution for any of the samples used in this study. During AF demagnetization of M_3 and M_4, none of the present results (Figs. 3 and 4) shows any remaining x-component after AF step $\tilde{H}_i$, confirming that high-coercivity tails are also absent for orthogonal pairs of pARMs.

AF demagnetization of M_3 for the 18.3 µm magnetite is replotted in the form of component decays in Fig. 9. Component x_3 decays quasi-exponentially over the expected range 0–30 mT, while z_3 decreases rather continuously over the entire 0–40 mT range. The scalar sum of x_3 and z_3 was compared to the predicted AF demagnetization based on the distribution of blocking and unblocking coercivity spectra $\chi^*(\tilde{H}_b, \tilde{H}_{UB})$ [11]. In order to construct a 3-D map of $\chi^*(\tilde{H}_b, \tilde{H}_{UB})$, pARM (5 mT, 0 mT) was produced and then
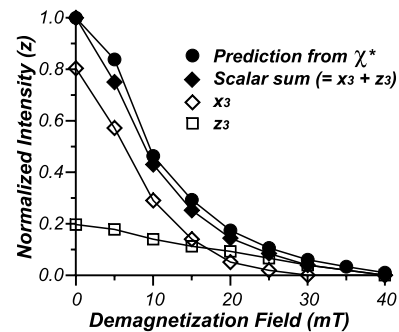

Fig. 9. A comparison of AF demagnetization of synthetic 18.3 µm sample for x_3, z_3, the sum x_3+z_3, and a prediction based on the experimentally determined distribution χ^*.

double AF demagnetization was performed to 5 mT in 2.5 mT steps. Next, pARM (10 mT, 5 mT) was produced and AF demagnetized to 10 mT. Similar pARMs were generated, incrementing the upper and lower limits of $\tilde{H}_b$ by 5 mT each time, and then AF demagnetized from 0 mT to the upper $\tilde{H}_b$. No pARMs with $\tilde{H}_b \geq 40$ mT were simulated because pARM (100 mT, 40 mT) is $< 2\%$ of total ARM intensity for the MD samples. We summed appropriate rows of χ^* parallel to the $\tilde{H}_b$ axis to find ARM remaining at a particular $\tilde{H}_{UB}$. Similarly addition of columns parallel to the $\tilde{H}_{UB}$ axis gave pARM acquisition for a given value of $\tilde{H}_b$. Since the unblocking coercivity fraction of $[\tilde{H}_{UB} < \tilde{H}_i]$ is affected similarly by the AF (see Section 6.1), whether it is acquisition of pARM$_x$ ($\tilde{H}_i$, 0) or AF demagnetization to $\tilde{H}_i$, we expect to observe the same AF demagnetization pattern for the scalar sum of x_3 and z_3 as we do for the decay predicted by χ^*. Fairly similar trends are indeed seen in Fig. 9, implying that construction of χ^* provides quantitative information on the orthogonal superposition of pARMs as well.

6.3. Multivectorial paleointensity determination

Failure to calculate correct paleointensities for H_a in Fig. 5 suggests an important lesson in paleointensity determination. The conventional Arai plot cannot yield reliable paleointensities for both H_b and H_a (Fig. 5a). Non-linear segments for H_b result from the ordinary calculation. This failure is curable using separated multivectorial Arai plots (Fig. 5b, left). However, the linear segment for the primary remanence always (except for $t = 1.0$) underestimates the primary field H_a because of violation of the independence law (Fig. 5a, insets). Using multivectorial Arai plots does not cure this problem (Fig. 5b, right). The slopes remain low by exactly the independence factor t. Therefore paleointensity determination for a primary remanence acquired in field H_a and subsequently overprinted by remanence in field H_b requires caution. In the multivectorial approach, paleointensity estimates for H_b are reliable but those for H_a are systematically underestimated.

Fig. 5a illustrates another important result for paleomagnetism. On vector projections, a sharp junction between adjacent remanences has generally been used to separate primary and remagnetization components of NRM. However, the vector plots for $t = 0.2$–0.8 failed to isolate correct directions for H_b (Fig. 5a) although they still preserve sharp junctions between H_a and H_b. Within experimental errors, $t = 0.8$–1.0 results are marginally acceptable but results for $t < 0.8$ definitely do not represent correct directions (dashed lines in vector plots). Thus, the direction of H_a is correctly recovered in multivectorial plots but the direction indicated for H_b increasingly deviates from the true direction as the degree of independence decreases.

In summary, for rocks whose primary remanence M_a (acquired in field H_a) has been overprinted, orthogonally or at large angle, by remanence M_b (acquired in a later field H_b), the estimated paleointensity for H_b and paleodirectional analysis for H_a are reliable but the estimated intensity for H_a would be underestimated and the estimated direction of H_b was deflected toward the direction of H_a unless the samples contain truly SD grains with fully independent partial remanences (Fig. 5). This is not normally tested. Instead vector plots with sharp junctions between linearly decaying components and (vector) Arai plots with linear segments are taken as diagnostic of ideal behavior. In multivectorial NRMs, such 'ideal' results can lead to spurious estimates of both paleodirections and paleointensities.

One may argue that considering $t < 1.0$ is unreasonable since ideal behavior in additivity and reciprocity were assumed at the outset. However, the assumption of ideality was made only for mathematical convenience. If we take PSD grains into consideration, the simulations become complicated. For instance, the convex-down rather than linear shapes of the Arai plots complicate matters and the vector projections lose their sharp junctions. However, the eventual conclusion of modeling would be similar: low estimates of the intensity H_a and spurious values of the direction of H_b.

The main difference between numerical simula-

tions and multivectorial paleointensity experiments is that numerical simulations predict a reliable paleointensity for H_b and an underestimated paleointensity for H_a, whereas in the experiments, estimated paleointensities for both H_b and H_a were reliable only for SD samples. For the PSD samples, H_b often could not be determined because of curvature of the Arai plots.

All the experimental and numerical results yielded linear plots for H_a, both on conventional and on vectorially separated Arai plots (Figs. 5–8). However, although the plots are linear and univectorial, their slopes definitely underestimate the true field (except for the SD sample) because of the violation of independence.

In practice, remagnetization may occur in any direction. Unfortunately, it is hard to quantify the outcome of remagnetization, especially when the overprinting occurs close to either parallel or antiparallel (magnetic field reversal) to the primary remanence. This is because in vector plots, the superimposed component is difficult to separate from the primary remanence unless they are at a reasonably large angle to each other.

The modeling and experimental results in Section 5 used orthogonal pARMs to test independence and its consequences. On the basis of the analogy between pARMs and pTRMs, we can anticipate that any violation of the independence of pTRMs will lead to similar problems. As Yu and Dunlop [14] point out, conventional rejection criteria for paleointensity determination have to be reconsidered, since linearity of the Arai plot and univectorial decay of NRM do not necessarily guarantee reliable paleointensities (or paleodirections). Experimental analyses and numerical modeling for multivectorial pARMs (this study) imply that SD grains can preserve reliable paleointensities while PSD grains often cannot. Violation of the independence law can lead to linear but unreliable results even in multivectorial Arai plots (Figs. 5–8). This fact leads to the prediction that paleointensities are increasingly underestimated as the grain size increases and the domain state becomes less SD-like. Since most paleointensity analyses in the literature have used samples containing PSD magnetites rather than strictly SD grains, there is a possibility that some of the lower

VADMs from overprinted rocks (which include many Precambrian rocks) are in fact underestimates.

7. Conclusion

1. The independence law of pARMs was tested by AF demagnetizing orthogonal pARMs whose blocking field intervals do not overlap with each other. For PSD and MD magnetites, the superimposed remanence substantially affected the pre-existing remanence, leading to a violation of independence.

2. In order to overcome the limitation of conventional Arai plots when used with multivectorial NRMs, we have introduced separate Arai plots for the individual vector components.

3. When a total ARM (simulating primary remanence in a field H_a) was orthogonally overprinted by pARM (simulating remagnetization in H_b), estimation of the intensity of H_b was relatively successful but the intensity of H_a was always underestimated. On the other hand, directional analysis of H_b was misleading while yielding an accurate direction for H_a. Violation of independence is responsible for these results. Determining accurate paleointensities and paleodirections for multivectorial NRMs requires additional reliability criteria.

References

[1] L. Tauxe, T. Pick, Y.S. Kok, Relative paleointensity in sediments: a pseudo-Thellier approach, Geophys. Res. Lett. 22 (1995) 2885–2888.

[2] Y.S. Kok, L. Tauxe, Saw-toothed pattern of sedimentary paleointensity records explained by cumulative viscous remanence, Earth Planet. Sci. Lett. 144 (1996) E9–E14.

[3] Y.S. Kok, L. Tauxe, Long-τ VRM and relative paleointensity estimates in sediments, Earth Planet. Sci. Lett. 168 (1999) 145–158.

[4] P.P. Kruiver, Y.S. Kok, M.J. Dekkers, C.G. Langereis, C. Laj, A pseudo-Thellier relative paleointensity record, and rock magnetic and geochemical parameters in relation to climate during the last 276 kyr in the Azores region, Geophys. J. Int. 136 (1999) 757–770.

[5] S.A. Brachfeld, S.K. Banerjee, A new high-resolution geomagnetic relative paleointensity record for the North American Holocene: A comparison of sedimentary and absolute intensity data, J. Geophys. Res. 105 (2000) 821–834.

[6] M. Cronin, L. Tauxe, C. Constable, P. Selkin, T. Pick, Noise in the quiet zone, Earth Planet. Sci. Lett. 190 (2001) 13–30.

[7] Y. Pan, R. Zhu, J. Shaw, Q. Liu, B. Guo, Can relative paleointensities be determined from the normalized magnetization of the wind-blown loess of China?, J. Geophys. Res. 106 (2001) 19259–19269.

[8] E. Thellier, O. Thellier, Sur l'intensité du champ magnétique terrestre dans le passé historique et géologique, Ann. Geophys. 15 (1959) 285–376.

[9] E. Thellier, Sur l'aimantation des terres cuites et ses applications géophysiques, Ann. Inst. Phys. Globe Univ. Paris 16 (1938) 157–302.

[10] Y. Yu, D.J. Dunlop, Ö. Özdemir, Partial anhysteretic remanent magnetization in magnetite 1. Additivity, J. Geophys. Res. 107(B10), 2002, 10.1029/2001JB001249.

[11] Y. Yu, D.J. Dunlop, Ö. Özdemir, Partial anhysteretic remanent magnetization in magnetite 2. Reciprocity, J. Geophys. Res. 107(B10), 2002, 10.1029/2001JB001269.

[12] Y. Yu, Rock Magnetic and Paleomagnetic Experiments on Hemoilmenites and Titanomagnetites in Some Volcanic Rocks from Japan, M. Sc Thesis, University of Toronto, 1998, 24 pp.

[13] Y. Yu, D.J. Dunlop, Paleointensity determination on the late Precambrian Tudor Gabbro, southern Ontario, J. Geophys. Res. 106 (2001) 26331–26344.

[14] Y. Yu, D.J. Dunlop, Multivectorial paleointensity determination from the Cordova Gabbro, southern Ontario, Earth Planet. Sci. Lett. 203 (2002) 983–998.

[15] D.J. Dunlop, Paleomagnetism of Archean rocks from northwestern Ontario: 4. Burchell Lake granite, Wawa-Shebandowan Subprovince, Can. J. Earth Sci. 21 (1984) 1098–1104.

[16] D.J. Dunlop, L.D. Schutts, C.J. Hale, Paleomagnetism of Archean rocks from northwestern Ontario: 3. Rock magnetism of the Shelley Lake granite, Quetico Subprovince, Can. J. Earth Sci. 21 (1984) 879–886.

[17] T. Nagata, Y. Arai, K. Momose, Secular variation of the geomagnetic total force during the last 5000 years, J. Geophys. Res. 68 (1963) 5277–5281.